Title: Slip behaviors extracted from decadal seafloor geodesy after the Tohoku-oki earthquake

Authors: Shun-ichi Watanabe[1]*, Tadashi Ishikawa[1], Yuto Nakamura[1], Yusuke Yokota[2]

Affiliations:

[1]Hydrographic and Oceanographic Department, Japan Coast Guard; Chiyoda-ku, Tokyo, 100-8932, Japan.

[2]Institute of Industrial Science, University of Tokyo; Meguro-ku, Tokyo, 153-8505, Japan.

*Corresponding author. Email: s-watanabe@jodc.go.jp

Abstract: Investigations of the co- and postseismic processes of the 2011 Tohoku-oki earthquake provide essential information on the seismic cycle in the Japan Trench. Although various postseismic models have been proposed, no consensus has been reached, especially on the along-strike extensions of the main rupture due to the lack of conclusive evidence, even in the coseismic process. To capture aseismic behaviors that restrain coseismic rupture propagation, it is necessary to perform long-term postseismic geodetic observation on the seafloor. Here, we provide empirical evidence for aseismic afterslip on the rupture edges by decomposing elementary postseismic processes from decadal seafloor geodetic data. The results suggest that the tsunami-derived shallow coseismic slip should be adopted in the viscoelastic relaxation model to reasonably explain the spatiotemporal variation of seafloor deformation.

One-Sentence Summary: Spatiotemporal variation of seafloor movement indicates a widely spread tsunamigenic rupture followed by a downdip afterslip.

Main Text: The 2011 Tohoku-oki earthquake (M_w 9.0) caused trench-ward seafloor displacements of several tens of meters (*1, 2*), reaching about 50 m at the trench (*3*). Using seafloor geodetic data (*1, 2*), which can provide definitive evidence for a coseismic slip, an extremely large slip was estimated at the plate interface shallower than the hypocenter (Fig. 1) (*4–6*). However, the geodetic network in 2011 did not cover the near-trench region, for which there is thus no information. Tsunami data, which are sensitive to topographical changes of the seafloor, indicate that the tsunamigenic area was extended, especially in the northern (> 39 °N) and southern (~ 37 °N) areas along the trench (Fig. 1) (*7*). In contrast to the shallower portion, a consensus has been reached on the north-south fault spreading at depths near the hypocenter; almost all fault models produce similar results (*4, 5*). This implies that the rupture in 2011 did not progress to the northern region, even though M_w 8 earthquakes have historically occurred in this region (Fig. 1) (*8, 9*).

Investigations of the postseismic behaviors on the northern and southern regions outside the main rupture can provide essential information on how rupture propagation was restrained in a compact region despite the widely spread shallow slip. In general, a fault rupture causes viscoelastic relaxation in the asthenosphere and aseismic slip on the fault plane, which lead to transient crustal deformation (*10*). Postseismic geodetic data show the sum of these relaxation processes and interplate backslip due to the relocking of the fault. Clarifying the behavior of afterslip below the seafloor will contribute to the understanding of the frictional state of faults, slow earthquake activities, and the seismic cycle in this region. To extract the afterslip on the rupture edges, postseismic deformation sources should be decomposed. Because these sources have different decay times and deformation patterns (*10*), elementary processes can be decomposed using sufficiently long-term, high-frequency, and well-distributed geodetic data. Although the terrestrial Global Navigation Satellite System (GNSS) observation network has extremely high spatiotemporal resolution, it cannot easily decompose the transient processes because the two processes of interest cause similar trench-ward movements in onshore regions and thus cannot be distinguished from one another. In contrast, the viscoelastic and afterslip effects cause displacements in opposite directions on the seafloor above the main rupture, i.e., the landward and trench-ward directions, respectively. Therefore, seafloor geodetic observations can be used to decompose transient deformation sources despite their lower temporal resolution compared to that of terrestrial observations. For instance, previous studies detected postseismic landward movements larger than the subduction rate (~ 9 cm/year) (*11*) above the main rupture, whereas terrestrial geodetic sites showed trench-ward movements. This is conclusive evidence for the dominance of viscoelastic relaxation (*12–15*).

Quantitative postseismic models, based on geodetic results, that incorporate both viscoelastic and afterslip effects suggest that afterslip and rupture areas are spatially compartmentalized (*5, 13, 16–18*). Although these models indicate that afterslip reaches the shallowest part in the northern and/or southern marginal regions, this result is incompatible with the widely spread shallow rupture derived from tsunami data (*7*). This inconsistency arises from the absence of geodetic constraint for decomposing deformation sources due to insufficient spatiotemporal resolution and insufficient observation period (at most 5 years). It should be noted that despite the importance of coseismic slip as an input for postseismic relaxation modeling, tsunami-derived slip distributions are rarely adopted. To discuss the postseismic process in marginal regions, uncertainties in coseismic rupture models should be taken into account. In this study, decadal seafloor geodetic data that contain the temporal evolutions of surface velocity are used to decompose deformation sources. Based on the results, we clarify the co- and postseismic slip behaviors in the northern and southern parts of the source region.

To investigate the temporal evolution of seafloor crustal deformation, the Japan Coast Guard (JCG) regularly performs seafloor geodetic observations using GNSS-A, a combination of GNSS and acoustic ranging, in the Japan Trench region. We analyzed GNSS-A observation data obtained from March 2011 to June 2020 using newly developed analysis method (*19*). Because the GNSS-A observation frequency is as low as several times per year per site, only the average velocity over several years can be discussed. Thus, we extracted 3-year average velocities at six sites (KAMN, KAMS, MYGI, MYGW, FUKU, and CHOS) for the periods of 2011–2014, 2014–2017, and 2017–2020 with respect to the Eurasian plate of the NUVEL-1A model (*11*) (Table 1, Fig. 1). Note that data in the first period include the update from the previous study (*12*). Because the velocity changes in the last two periods were smaller than 2 cm/year except for the sites above the main rupture and there were no clear temporal changes, we use the average velocity in the period of 2014–2020 for comparison (Table 2, Fig. 1C). The JCG also performs GNSS-A observations at five sites (G08, G10, G12, G14, and G17) installed by Tohoku University (TU) (*20*), independently of TU (*19*). The observations at the TU sites started in 2013 and are less frequent than those at the other sites. Thus, only the 2014–2020 average velocities were considered for these sites (Table 2, Fig. 1C). We additionally reprocessed the GNSS-A data before the event at five sites (*21*) using the present analysis method (*19*) to determine the preseismic seafloor velocities (Table 1, Fig. 1A). Based on the temporal changes of seafloor velocity (Fig. 1B and C), we discuss the expressions of viscoelastic relaxation and afterslip in the northern, central, and southern parts of the source region, which are conceptually summarized in Fig. 2.

In previous studies that analyzed the data until 2014 (*12, 13*), landward movements at rates larger than the Pacific plate subduction were detected at the sites located above the main rupture, i.e., KAMS and MYGI (Fig. 1B). This was interpreted as the superposition of the effects of viscoelastic relaxation in the asthenosphere beneath the Pacific plate and the interplate backslip (Fig. 2), though the restoration of interplate coupling could not be resolved. Restored interplate coupling would cause a landward motion as large as the preseismic velocity (Fig. 2C), which is insufficient to reproduce the postseismic motion. Crustal deformation in this area was consistent with the quantitative models of the viscoelastic response to the geodetically constrained coseismic input (*5, 13, 16, 18*). The large landward movements at these sites continued with a slight decay even after 2014, as well as at G08, G10, G12, and G14 (Fig. 1C). The decay of landward motion can be explained as time-dependent viscoelastic deformation (Fig. 2C).

Little temporal change in the present decade was found in the horizontal movement at MYGW on the downdip edge of the main rupture (Fig. 1B and C). If interplate coupling in the main rupture had been restored, its landward motion should be canceled by a trench-ward motion driven by viscoelastic relaxation or afterslip to maintain balance for almost 10 years. Although the landward motion cannot be clearly detected, it seems to have been slightly restored after 2017. This might indicate a decrease in the dominance of relaxation processes similar to those in the main rupture area (Fig. 2C).

At the northern edge of the main rupture, little horizontal displacement was observed until 2014 at KAMN (Fig. 1B). Because viscoelastic relaxation is mainly driven by the stress induced in the low-viscosity layer beneath the lithosphere, it tends to cause almost the same movements in a narrow region. To explain the velocity contrast at KAMN and KAMS, some postseismic models make afterslip reach the trench on the northern side of the main rupture to cause a relative trench-ward motion at KAMN with respect to KAMS (*16, 18*).

After 2014, landward motion significantly accelerated and had almost the same velocity at KAMS and MYGI (Fig. 1C). With the preseismic velocities (Fig. 1A) taken into account, the consistency in the movements at KAMN and KAMS after 2014 indicates that the two sites have been similarly influenced by long-term viscoelastic relaxation. Because the spatial pattern of the viscoelastic deformation has not significantly changed in the present decade, the viscoelastic relaxation is expected to have caused almost the same displacements at these sites before 2014. This supports that the northern afterslip caused the relative trench-ward motion of 10 cm/year at KAMN before 2014 to cancel the landward motion driven by the viscoelastic relaxation and relocking (Fig. 2C). Furthermore, the data after 2014 confirms that the northern afterslip had decayed sufficiently in 3 years. After the decay of the afterslip, the viscoelastic response and interplate coupling became dominant for the crustal deformation around KAMN, similar to the case at neighboring GNSS-A sites (Fig. 2B and C).

To reproduce the velocity difference of 10 cm/year between KAMN and KAMS before 2014, afterslip in the north region outside the coseismic rupture with an average displacement rate of 1–3 m/y is required (*22*). The slip magnitude depends on the spread of the afterslip region, which cannot be geodetically constrained. With the tsunami-derived shallow slip in the northern area taken into account, afterslip would not have reached the trench at 39 °N (Fig. 1B).

In contrast to the central region, trench-ward movements were observed in the southern region (< 37.5 °N) before 2014 (Fig. 1B). Several postseismic models suggested that the rapid trench-ward and downward motion at FUKU is caused by afterslip on the shallower portion, because neither afterslip beneath the coast nor viscoelastic deformation driven by geodetically derived coseismic inputs with a single peak beneath FUKU, such as the model by Iinuma et al. (*6*) (Fig. 1B), can reproduce the result (*16*–*18*).

The trench-ward motion became much smaller after 2014 (Fig. 1C). Almost the same trend was found at G17, located on the trench side of FUKU, despite the low accuracy due to instrumental malfunction (*19*). Nonetheless, even after 2014, when the trench-ward movement had almost ceased, subsidence continued at almost a constant rate of about 4 cm/year at FUKU. A single afterslip is inadequate to cause persistent subsidence without significant trench-ward movement at FUKU and G17 because of the low dip angle of the plate boundary. Although the previous viscoelastic models showed the insufficiency of causing the observed subsidence, they have uncertainty in the coseismic input. Therefore, we should discuss how the viscoelastic response can reproduce the observed decadal surface deformation.

The viscoelastic finite element model proposed by Agata et al., which incorporates the additional peak of coseismic rupture near the trench at 37 °N, demonstrated sufficient subsidence at FUKU (*23*). The tsunami-derived coseismic slip distribution in the off-Fukushima region (*7*) has two peaks in the along-dip direction (Fig. 1B). Based on the postseismic model (*23*), the viscoelastic relaxation driven by the shallower coseismic slip can cause long-term subsidence at FUKU (red arrows in Fig. 2C). In this case, both the viscoelastic relaxation and possible relocking simultaneously cause significant landward motion at G17 (red and yellow arrows in Fig. 2C, respectively), which is inconsistent with the observation. Accordingly, the observation result at G17 requires an afterslip on the downdip side of the shallow rupture (purple area in Fig. 2B) to cancel the landward motion (purple arrow in Fig. 2C). Recalling the tsunami-derived rupture distribution at 37 °N, it is reasonable to put the southern afterslip on the fault between the two peaks of the coseismic slip (Fig. 1B).

Unlike the northern afterslip, this should continue even after 2014 according to the result at G17, although this is dependent on the observation accuracy.

The assumed afterslip regions on the northern and southern sides of the main rupture are considered to have behaved as barriers to rupture propagation. It is plausible that the shallow tsunamigenic slip in the northern and southern areas (*7*) loaded stress and triggered afterslip on the downdip side. Northern afterslip occurred between major earthquakes, i.e., the 1968 Tokachi-oki earthquake (M_w 8.3), the 1994 offshore Sanriku earthquake (M_w 7.7) (*8*), the 1896 Meiji Sanriku tsunami earthquake (M_w 8.1) (*24*), and the 2011 Tohoku-oki earthquake. The gap between major earthquakes is characterized by relatively low seismicity (*25*), including repeating earthquakes (*26, 27*). Slow earthquake activity has been reported in this area (*28*). Although the northern and along-dip extensions cannot be resolved due to the absence of geodetic instruments, these features support the aseismic frictional property of the plate interface in this region. In the off-Fukushima region, postseismic movements larger than the main slip were observed for the 2008 and 2010 Fukushima-ken-oki earthquakes (M_j 6.9 and M_j 6.7, respectively) (*29*). It is possible that the proposed southern afterslip following the Tohoku-oki earthquake occurred in a region near the former afterslip.

Based on the GNSS-A observations and the above interpretations, the slip behaviors in the northern and southern areas can be summarized as follows. (1) Afterslip occurred in the northern and southern regions outside the main rupture at depths near the hypocenter, which is consistent with the shallower tsunamigenic slip inducing stress on the downdip aseismic faults. It is plausible that these aseismic afterslip regions stopped north-south rupture propagation. (2) The afterslip in the southern region might still be ongoing, whereas that in the northern region almost ceased in around 2014. (3) Shallow tsunamigenic slip in the south was captured by postseismic seafloor geodesy as a subsequent viscoelastic deformation that caused persistent seafloor subsidence. Additionally, the GNSS-A results indicate that the long-term viscoelastic relaxation process is currently in progress and is dominant in the central and northern regions. It also plays an important role in the southern region, although its contribution cannot be well resolved. These long-term behaviors should be investigated by continuing and expanding seafloor geodetic observations.

References and Notes

1. M. Sato, T. Ishikawa, N. Ujihara, S. Yoshida, M. Fujita, M. Mochizuki, A. Asada, Displacement above the hypocenter of the 2011 Tohoku-oki earthquake. *Science* **332**, 1395 (2011).
2. M. Kido, Y. Osada, H. Fujimoto, R. Hino, Y. Ito, Trench-normal variation in observed seafloor displacements associated with the 2011 Tohoku-Oki earthquake. *Geophys. Res. Lett.* **38**, L24303 (2011).
3. T. Fujiwara, S. Kodaira, T. No, Y. Kaiho, N. Takahashi, Y. Kaneda, The 2011 Tohoku-Oki earthquake: displacement reaching the trench axis. *Science* **334**, 1240 (2011).
4. T. Sun, K. Wang, T. Fujiwara, S. Kodaira, J. He, Large fault slip peaking at trench in the 2011 Tohoku-oki earthquake. *Nat. Commun.* **8**, 14044 (2017).
5. K. Wang, T. Sun, L. Brown, R. Hino, F. Tomita, M. Kido, T. Iinuma, S. Kodaira, T. Fujiwara, Learning from crustal deformation associated with M9 2011 Tohoku-oki earthquake. *Geosphere* **14**, 552–571 (2018).
6. T. Iinuma, R. Hino, M. Kido, D. Inazu, Y. Osada, Y. Ito, M. Ohzono, H. Tsushima, S. Suzuki, H. Fujimoto, S. Miura, Coseismic slip distribution of the 2011 off the Pacific Coast of Tohoku

Earthquake (M9.0) refined by means of seafloor geodetic data. *J. Geophys. Res.* **117**, B07409 (2012).

7. K. Satake, Y. Fujii, T. Harada, Y. Namegaya, Time and space distribution of coseismic slip of the 2011 Tohoku earthquake as inferred from tsunami waveform data. *Bull. Seismol. Soc. Am.* **103**, 1473–1492. (2013).
8. R. Nagai, M. Kikuchi, Y. Yamanaka, Comparative study on the source processes of recurrent large earthquakes in Sanriku-oki Region: The 1968 Tokachi-oki earthquake and the 1994 Sanriku-oki earthquake, *Zisin(2)*, **54**, 267-280, (2001).
9. Y. Yamanaka, M. Kikuchi, Asperity map along the subduction zone in northeastern Japan inferred from regional seismic data. *J. Geophys. Res.* **109**, B07307 (2004).
10. K. Wang, Y. Hu, J. He, Deformation cycles of subduction earthquakes in a viscoelastic Earth. *Nature* **484**, 327–332 (2012).
11. C. DeMets, R. G. Gordon, D. F. Argus, S. Stein, Effect of recent revisions to the geomagnetic reversal time scale on estimates of current plate motions, *Geophys. Res. Lett.* **21**, 2191-2194, (1994).
12. S. Watanabe, M. Sato, M. Fujita, T. Ishikawa, Y. Yokota, N. Ujihara, A. Asada, Evidence of viscoelastic deformation following the 2011 Tohoku-oki earthquake revealed from seafloor geodetic observation. *Geophys. Res. Lett.* **41**, 5789–5796 (2014).
13. T. Sun, K. Wang, T. Iinuma, R. Hino, J. He, H. Fujimoto, M. Kido, Y. Osada, S. Miura, Y. Ohta, Y. Hu, Prevalence of viscoelastic relaxation after the 2011 Tohoku-oki earthquake. *Nature* **514**, 84–87 (2014).
14. F. Tomita, M. Kido, Y. Ohta, T. Iinuma, R. Hino, Along-trench variation in seafloor displacements after the 2011 Tohoku earthquake. *Sci. Adv.* **3**, e1700113 (2017).
15. C. Honsho, M. Kido, F. Tomita, N. Uchida, Offshore postseismic deformation of the 2011 Tohoku earthquake revisited: application of an improved GPS-acoustic positioning method considering horizontal gradient of sound speed structure. *J. Geophys. Res. Solid Earth* **124**, 5990–6009 (2019).
16. T. Sun, K. Wang, Viscoelastic relaxation following subduction earthquakes and its effects on afterslip determination. *J. Geophys. Res.* **120**, 1329–1344 (2015).
17. T. Iinuma, R. Hino, N. Uchida, W. Nakamura, M. Kido, Y. Osada, S. Miura, Seafloor observations indicate spatial separation of coseismic and postseismic slips in the 2011 Tohoku earthquake. *Nat. Commun.* **7**, 13506 (2016).
18. A. M. Freed, A. Hashima, T. W. Becker, D. A. Okaya, H. Sato, Y. Hatanaka, Resolving depth-dependent subduction zone viscosity and afterslip from postseismic displacements following the 2011 Tohoku-Oki, Japan earthquake. *Earth Planet. Sci. Lett.* **459**, 279–290 (2017).
19. See supplementary materials.
20. M. Kido, H. Fujimoto, R. Hino, Y. Ohta, Y. Osada, T. Iinuma, R. Azuma, I. Wada, S. Miura, S. Suzuki, F. Tomita, M. Imano, “Progress in the project for development of GPS/Acoustic technique over the last 4 years” in *International Symposium on Geodesy for Earthquake and Natural Hazards (GENAH)*, M. Hashimoto, Ed. (Springer, 2015), pp. 3–10.

21. M. Sato, M. Fujita, Y. Matsumoto, T. Ishikawa, H. Saito, M. Mochizuki, A. Asada, Interplate coupling off northeastern Japan before the 2011 Tohoku-oki earthquake, inferred from seafloor geodetic data. *J. Geophys. Res.* **118**, 3860–3869 (2013).

22. Y. Okada, Internal deformation due to shear and tensile faults in a half-space. *Bull. Seism. Soc. Am.* **82**, 1018-1040. (1992).

23. R. Agata, S. D. Barbot, K. Fujita, M. Hyodo, T. Iinuma, R. Nakata, T. Ichimura, T. Hori, Rapid mantle flow with power-law creep explains deformation after the 2011 Tohoku mega-quake. *Nat. Commun.* **10**, 1385 (2019).

24. K. Satake, Y. Fujii, S. Yamaki, Different depths of near-trench slips of the 1896 Sanriku and 2011 Tohoku earthquakes. *Geosci. Lett.* **4**, 33. (2017).

25. K. Mochizuki, M. Nakamura, J. Kasahara, R. Hino, M. Nishino, A. Kuwano, Y. Nakamura, T. Yamada, M. Shinohara, T. Sato, P. P. Moghaddam, T. Kanazawa, Intense PP reflection beneath the aseismic forearc slope of the Japan Trench subduction zone and its implication of aseismic slip subduction, *J. Geophys. Res.* **110**, B01302 (2005).

26. N. Uchida, T. Matsuzawa, Pre- and postseismic slow slip surrounding the 2011 Tohoku-oki earthquake rupture. *Earth Planet. Sci. Lett.* **374**, 81–91 (2013).

27. T. Igarashi, Catalog of small repeating earthquakes for the Japanese Islands. *Earth Planet. Space* **72**, 73 (2020).

28. T. Nishikawa, T. Matsuzawa, K. Ohta, N. Uchida, T. Nishimura, S. Ide, The slow earthquake spectrum in the Japan Trench illuminated by the S-net seafloor observatories. *Science* **365**, 808–813 (2019).

29. H. Suito, T. Nishimura, M. Tobita, T. Imakiire, S. Ozawa, Interplate fault slip along the Japan Trench before the occurrence of the 2011 off the Pacific coast of Tohoku Earthquake as inferred from GPS data, *Earth Planet. Space* **63**, 615–619 (2011).

30. H. Nakagawa, T. Toyofuku, K. Kotani, B. Miyahara, C. Iwashita, S. Kawamoto, Y. Hatanaka, H. Munekane, M. Ishimoto, T. Yutsudo, N. Ishikura, Y. Sugawara, Development and validation of GEONET new analysis strategy (Version 4). *J. Geogr. Surv. Inst.* **118**, 1–8 (2009).

31. S. Watanabe, T. Ishikawa, Y. Yokota, Y. Nakamura, GARPOS: Analysis Software for the GNSS-A seafloor positioning with simultaneous estimation of sound speed structure, *Front. Earth Sci.* **8**, 597532 (2020).

32. S. Watanabe, T. Ishikawa, Y. Yokota, Y. Nakamura, GARPOS: Analysis tool for GNSS-Acoustic seafloor positioning (Version 1.0.0). Zenodo (2021); https://doi.org/10.5281/zenodo.4522027.

33. S. Watanabe, T. Ishikawa, Y. Nakamura, Y. Yokota, GNSS-A data obtained at the sites along the Japan Trench before the 2011 Tohoku-oki earthquake (Version 1.0.0). Zenodo (2021); https://doi.org/10.5281/zenodo.4528990.

34. S. Watanabe, T. Ishikawa, Y. Nakamura, Y. Yokota, GNSS-A data obtained at the sites along the Japan Trench before the 2011 Tohoku-oki earthquake (Version 1.0.0). Zenodo (2021); https://doi.org/10.5281/zenodo.4529008.

35. M. Sato, M. Fujita, Y. Matsumoto, H. Saito, T. Ishikawa, T. Asakura, Improvement of GPS/acoustic seafloor positioning precision through controlling the ship's track line, *J. Geod.* **118**, 1–10 (2013).

36. T. Ishikawa, Y. Yokota, S. Watanabe, Y. Nakamura, History of on-board equipment improvement for GNSS-A observation with focus on observation frequency, *Front. Earth Sci.* **8**, 150 (2020).

37. Y. Nakamura, T. Ishikawa, Y. Yokota, S. Watanabe, Optimal transponder array and survey line configurations for GNSS-A observation evaluated by numerical simulation, *Front. Earth Sci.* **9**, 600993 (2021).

Acknowledgments: We would like to thank M. Kido of the Tohoku University for allowing us to use their seafloor geodetic instruments, i.e., G08, G10, G12, G14 and G17. In-situ observations were performed by the survey vessels operated by the Japan Coast Guard.

Funding:

Japan Coast Guard (SW, TI, YN)

The University of Tokyo Excellent Young Researcher project (YY)

Author contributions:

Conceptualization: SW, TI, YY

Methodology: SW, TI, YN, YY

Software: SW

Formal analysis: SW, YN

Investigation: SW, TI, YN, YY

Visualization: SW

Writing – original draft: SW

Writing – review & editing: SW, TI, YN, YY

Competing interests: Authors declare that they have no competing interests.

Data and materials availability: The dataset generated during this study are included in the Supplementary Materials. The GNSS-A analysis software "GARPOS v1.0.0" is available at Zenodo (*32*). The GNSS-A data is available at Zenodo (*33, 34*). The daily coordinates of terrestrial GNSS sites were provided by the Geospatial Information Authority of Japan (http://terras.gsi.go.jp) (*30*). The contours for some earthquakes were obtained from the website created by N. Uchida (https://www.aob.gp.tohoku.ac.jp/~uchida/page_3_asp-e.html). Some figures were prepared using Generic Mapping Tools (https://www.generic-mapping-tools.org/).

Supplementary Materials

Materials and Methods

Figs. S1 to S4

References (*31–37*)

Data S1 to S2

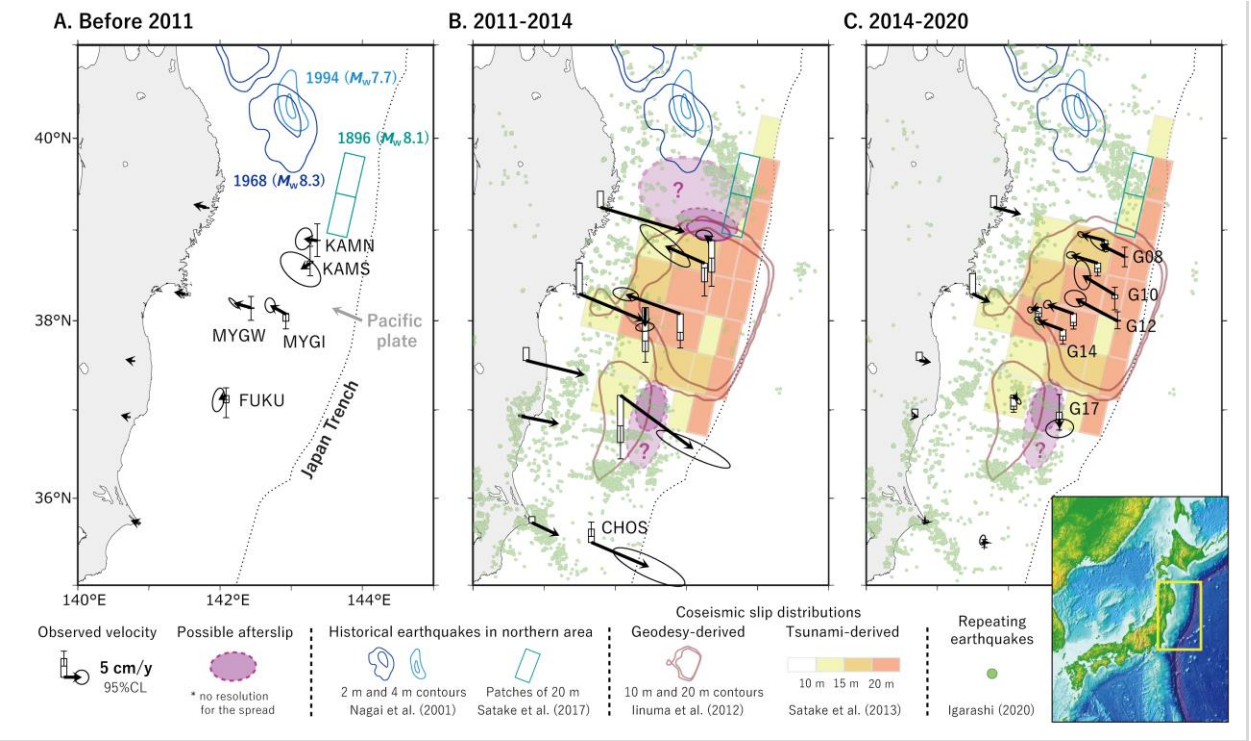

Fig. 1. Seafloor motion derived from GNSS-A observations. Average horizontal and vertical velocities for (**A**) pre-seismic period, (**B**) 2011–2014, and (**C**) 2014–2020 are indicated as black arrows and open rectangles, respectively. Terrestrial GNSS velocities were extracted from the F3 solution for GEONET sites (*30*). Onshore velocities during 2007–2011 are shown in (**A**). Purple patches indicate possible afterslip regions. Brown contours and colored tiles indicate geodetically derived (*6*) and tsunami-derived (*7*) coseismic slip distributions of the 2011 Tohoku-oki earthquake, respectively. Green circles in (**B**) and (**C**) denote repeating earthquakes that occurred in each period (*27*). Navy and blue lines indicate 2-m and 4-m slip contours of historical earthquakes in the northern area (*8*). Green rectangles indicate patches with a slip of 20 m for the 1896 tsunami earthquake (*24*).

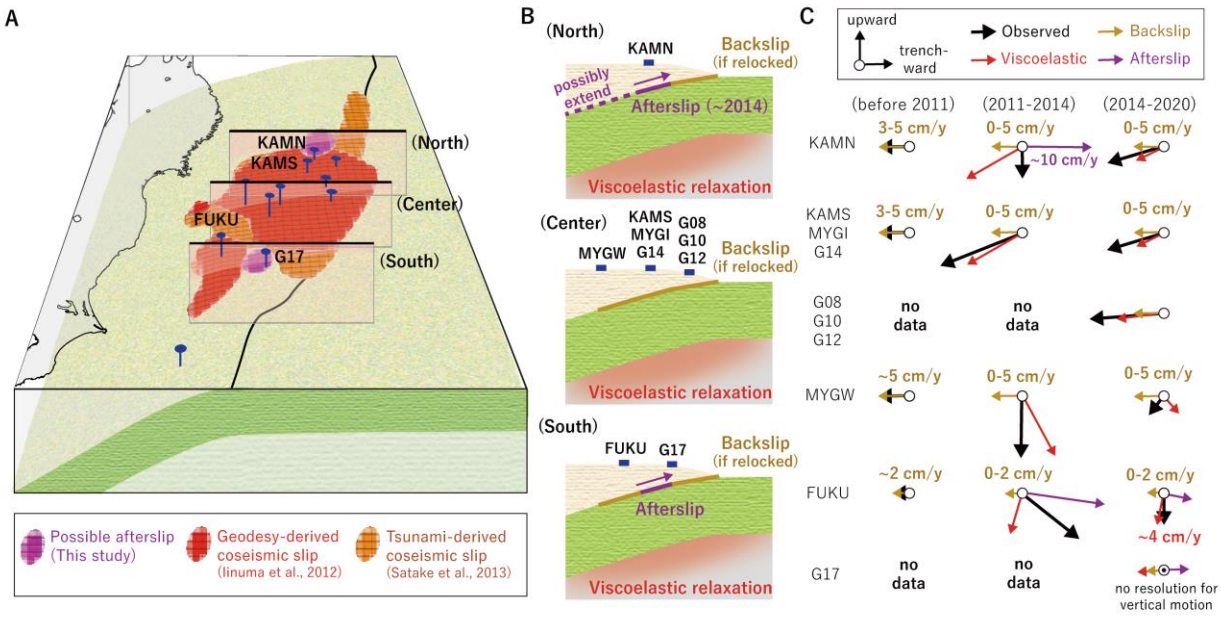

Fig. 2. Schematic diagram of deformation sources beneath the seafloor. (**A**) Slips on the plate interface. Purple, red, and orange regions indicate possible afterslip region and geodetically derived (*6*) and tsunami-derived (*7*) coseismic slip areas of the 2011 Tohoku-oki earthquake, respectively. Blue circles and bars indicate the locations of GNSS-A sites and their projections to the plate interface, respectively. Black rectangles show the locations for cross sections illustrated in subsequent panels. (**B**) Cross sections of northern (top), central (middle), and southern regions (bottom). (**C**) Qualitative explanations for the contributions of each deformation source to the motion at GNSS-A sites. Black, red, purple, and yellow arrows indicate the observed motion and components due to viscoelastic relaxation, afterslip, and interplate coupling, respectively.

Table 1. Three-year average displacement rates with 95% confidence intervals.

Site	Period	Eastward [cm/year]	Northward [cm/year]	Upward [cm/year]
KAMN	Pre-2011	−3.8 +/− 1.8	0.5 +/− 2.3	0.1 +/− 4.5
	2011–2014	−2.1 +/− 1.7	1.5 +/− 1.1	−8.7 +/− 3.9
	2014–2017	−6.4 +/− 1.9	2.0 +/− 1.8	−0.9 +/− 2.0
	2017–2020	−7.6 +/− 2.2	2.4 +/− 1.7	−1.4 +/− 2.5
KAMS	Pre-2011	−2.7 +/− 4.2	−1.7 +/− 3.6	0.7 +/− 4.0
	2011–2014	−11.1 +/− 5.4	4.9 +/− 4.6	−5.1 +/− 3.9
	2014–2017	−10.0 +/− 1.8	2.3 +/− 2.9	−0.4 +/− 1.3
	2017–2020	−6.3 +/− 2.8	2.7 +/− 1.6	−1.2 +/− 2.9
MYGI	Pre-2011	−4.4 +/− 1.1	2.5 +/− 1.6	−2.0 +/− 2.1
	2011–2014	−15.4 +/− 2.8	5.5 +/− 1.4	−7.3 +/− 2.2
	2014–2017	−8.8 +/− 1.4	1.6 +/− 1.6	−0.9 +/− 2.5
	2017–2020	−6.0 +/− 2.6	3.7 +/− 2.8	−4.5 +/− 2.3
MYGW	Pre-2011	−4.8 +/− 1.1	1.3 +/− 1.1	−0.2 +/− 3.3
	2011–2014	−0.1 +/− 2.0	−5.4 +/− 1.0	−12.2 +/− 3.0
	2014–2017	−1.2 +/− 1.9	−1.0 +/− 1.5	0.0 +/− 1.8
	2017–2020	−2.4 +/− 1.3	0.6 +/− 1.7	−1.3 +/− 2.0
FUKU	Pre-2011	−2.1 +/− 1.3	−1.2 +/− 2.5	−2.0 +/− 4.2
	2011–2014	20.5 +/− 8.0	−15.1 +/− 4.1	−13.3 +/− 4.6
	2014–2017	1.8 +/− 1.2	−1.9 +/− 1.7	−2.1 +/− 3.4
	2017–2020	0.2 +/− 1.3	−0.2 +/− 1.7	−3.8 +/− 1.7
CHOS	Pre-2011	N/A	N/A	N/A
	2011–2014	16.2 +/− 7.7	−6.9 +/− 4.2	3.8 +/− 2.1
	2014–2017	−1.1 +/− 1.8	0.1 +/− 1.5	−0.0 +/− 6.3
	2017–2020	−1.2 +/− 1.3	−0.3 +/− 2.4	0.7 +/− 2.1

Table 2. Average displacement rates in the period of 2014–2020 with 95% confidence intervals.

Site	Eastward [cm/year]	Northward [cm/year]	Upward [cm/year]
KAMN	−6.7 +/− 0.7	1.6 +/− 0.6	−1.7 +/− 0.8
KAMS	−7.5 +/− 1.0	2.3 +/− 0.7	−2.5 +/− 1.0
MYGI	−7.3 +/− 0.8	2.7 +/− 0.9	−3.3 +/− 0.9
MYGW	−2.3 +/− 0.6	−0.7 +/− 0.7	−2.6 +/− 0.9
FUKU	1.3 +/− 0.6	−1.6 +/− 0.8	−3.9 +/− 0.9
CHOS	−0.6 +/− 0.6	0.7 +/− 1.1	−0.3 +/− 1.2
G08	−7.1 +/− 2.0	3.5 +/− 1.6	−0.1 +/− 2.7
G10	−9.1 +/− 1.8	5.5 +/− 3.2	−1.0 +/− 3.1
G12	−11.9 +/− 2.4	6.3 +/− 1.8	0.2 +/− 2.3
G14	−6.9 +/− 0.8	2.6 +/− 0.8	−2.8 +/− 1.1
G17	0.1 +/− 3.0	−2.6 +/− 2.0	2.0 +/− 5.0

Supplementary Materials for

Slip behaviors extracted from decadal seafloor geodesy after the Tohoku-oki earthquake

Shun-ichi Watanabe*, Tadashi Ishikawa, Yuto Nakamura, Yusuke Yokota

Correspondence to: s-watanabe@jodc.go.jp

This PDF file includes:

Materials and Methods
Figs. S1 to S4
Captions for Data S1 and S2

Other Supplementary Materials for this manuscript include the following:

Data S1 and S2 (.xlsx format)

Materials and Methods

GNSS-A data and processing

GNSS-A data used in this study are obtained using the survey vessels of Japan Coast Guard (JCG) and are processed with GARPOS v1.0.0 (*31, 32*) (Fig. S1). All GNSS-A data used in this study are available at Zenodo (*33*) and (*34*) for pre- and postseismic data, respectively. Note that the GNSS-A data before 2009 were obtained by drifting observations, which were less precise than the recent results (*35, 36*) (Fig. S1A).

Time series of post- and preseismic seafloor displacements with respect to the Eurasian plate of NUVEL-1A model (*11*) are shown in Fig. S2 and Fig. S3, respectively. The values of the displacement are available in Data S1 and S2. The GNSS-A results at the same sites independently operated by the group of the Tohoku University (*15, 20*) are simultaneously plotted in Fig. S2 (G)–(K). The offsets in the results between two observation systems, i.e., JCG and Tohoku University (TU) were estimated and corrected as follows: We first estimated the linear trend of JCG's results in the period of 2013-2017, and detrended both series. Offsets were calculated from the average of differences in the detrended results for 2013–2017.

Validations and reasons for the lower precision at G17

Previous study (*15*) performed by the TU research group showed an average velocity of approximately 10 cm/year toward the trench at G17 in a period between 2012 and 2016 and is consistent with our results of the period after 2014, which we are discussing in this study. On the other hand, the results at G17 showed lower precision than other sites. There should be several reasons as follows: Firstly, mirror transponders installed at G17 frequently misrecognized their identification numbers for acoustic ranging, which are necessary to distinguish the transponder that responded to the acoustic signal. Secondly, some of the on-board system were unable to perform acoustic ranging longer than 10 seconds so that the track line had to be shrunken, until restoration in 2019 (Fig. S4). In practice, lack of acoustic data from the outside of the transponder array significantly degrades the positioning accuracy (*37*). These errors were also occurred at G12, but G17 seemed more significantly affected. The difference between G12 and G17 might be caused by the transponder arrangement or the complexity in the seawater sound speed structure. Although we cannot quantify the positioning accuracy, the results from late 2016 to 2018 tend to contain larger uncertainty.

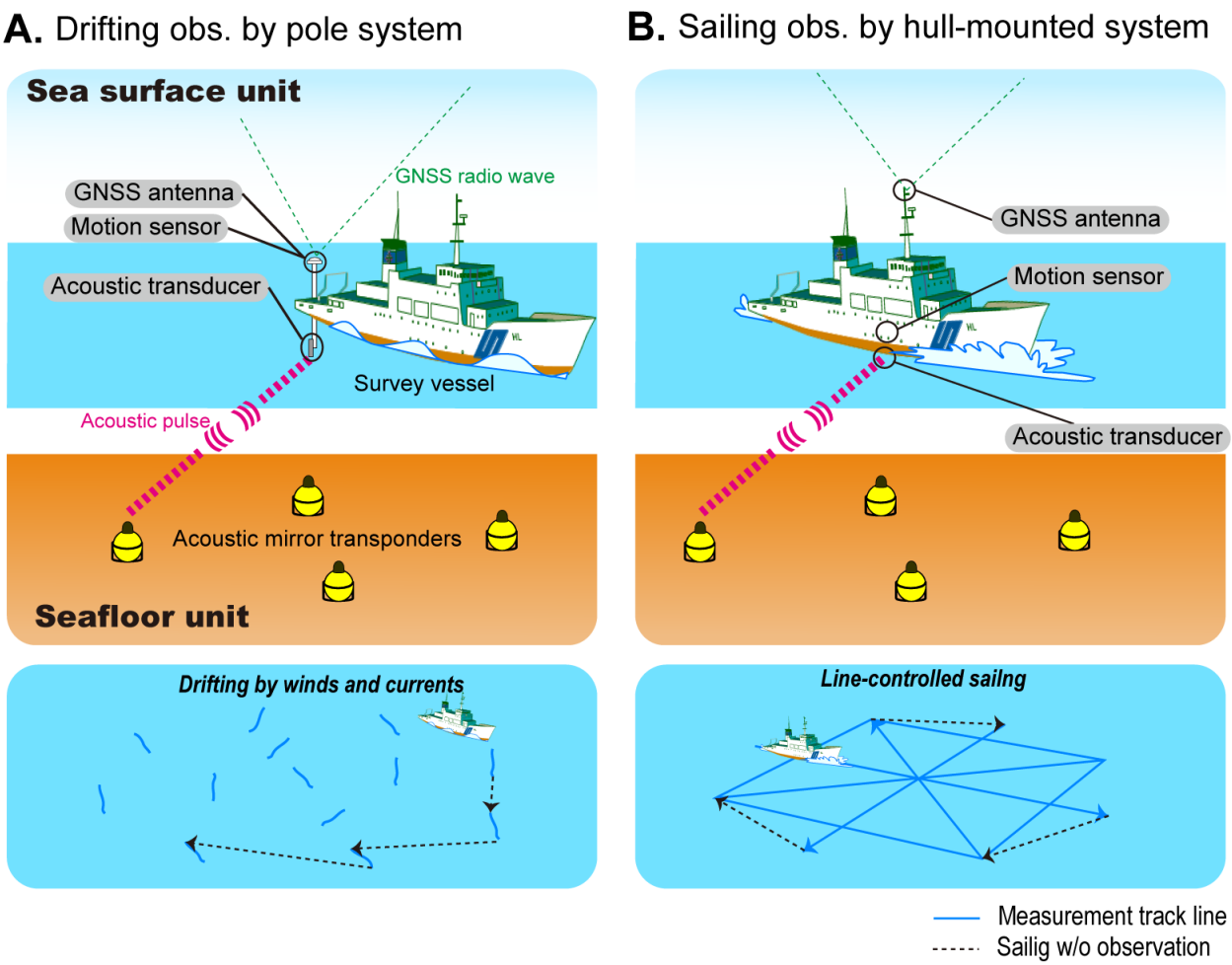

Fig. S1. Schematic pictures of the GNSS-A observation. Observation configurations for (A) drifting and (B) sailing systems are shown. Figures were modified from Ishikawa et al. (*36*).

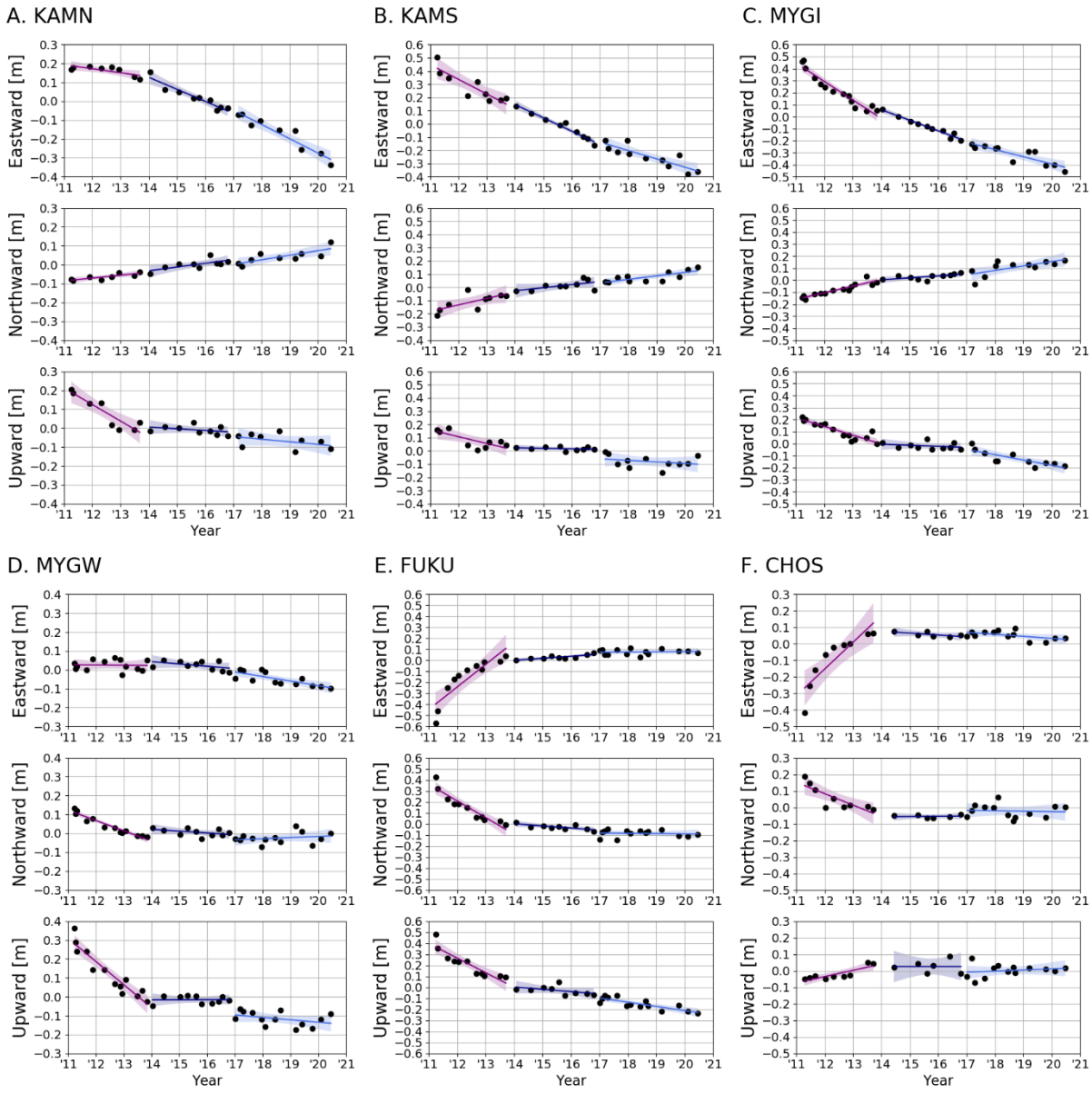

Fig. S2. Time series of postseismic seafloor displacement. Displacements with respect to the Eurasian plate of NUVEL-1A model (*11*) are shown (black circles). Three-year average velocities for (A)–(F), and six-year average velocities for (G)–(K) are shown as the solid lines. The 95 % confidence intervals for the average velocities are shown as the shaded areas. Results provided by Honsho et al. (*15*) for (G)–(K) are indicated as brown squares.

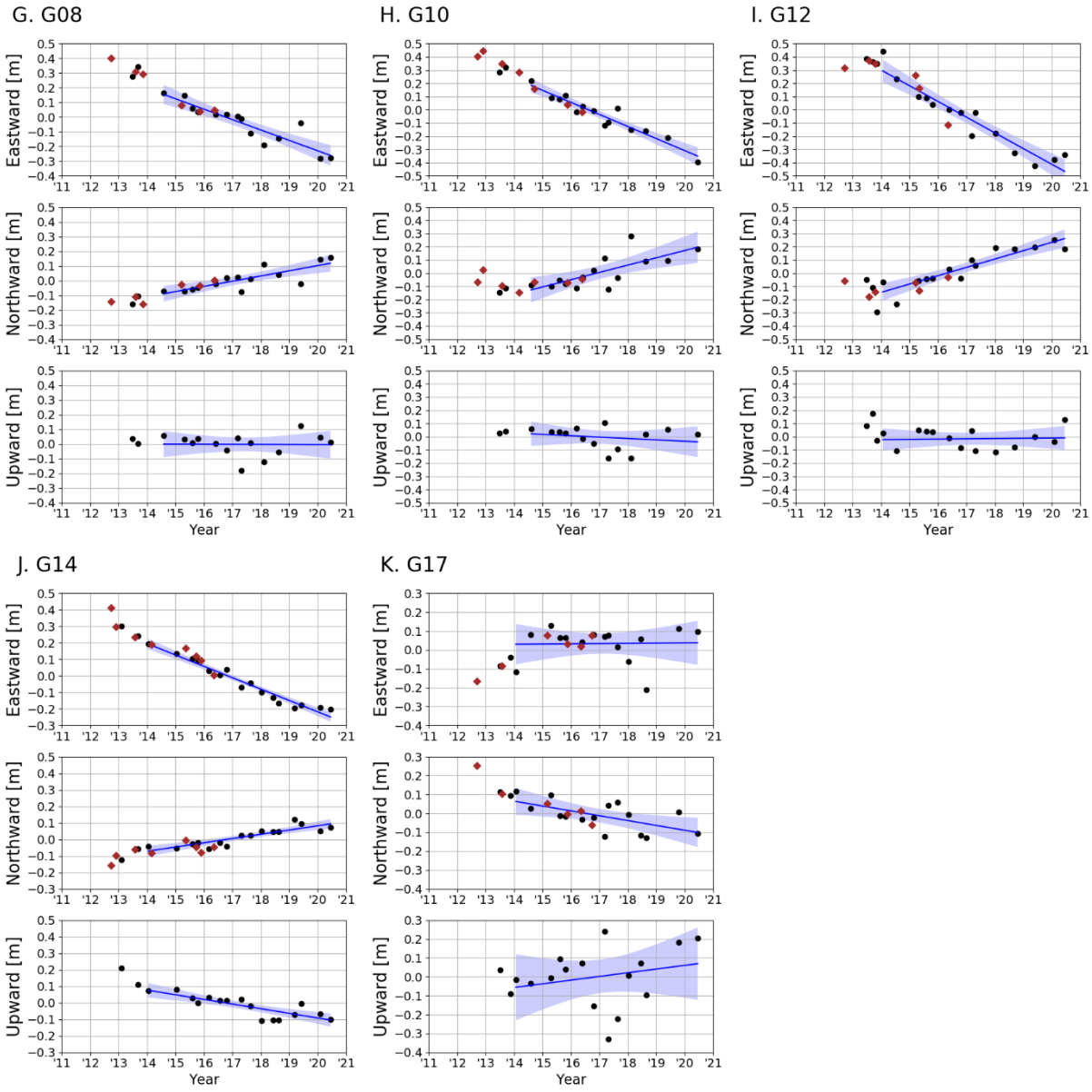

Fig. S2. Time series of seafloor displacement (continued).

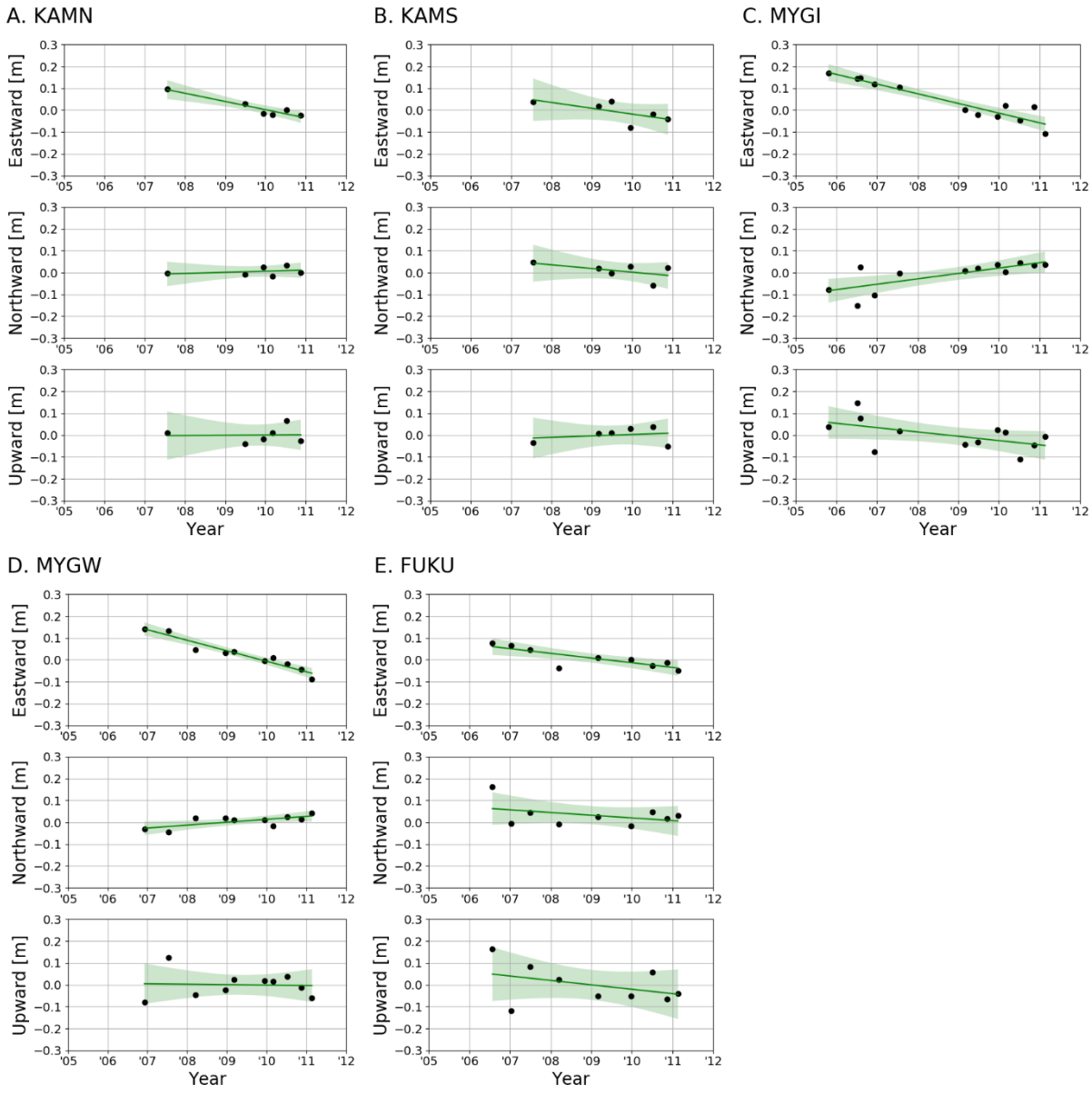

Fig. S3. Time series of preseismic seafloor displacement. Displacements with respect to the Eurasian plate of NUVEL-1A model (*11*) are shown (black circles). Average velocities and their 95 % confidence intervals are shown as the solid lines and shaded areas, respectively.

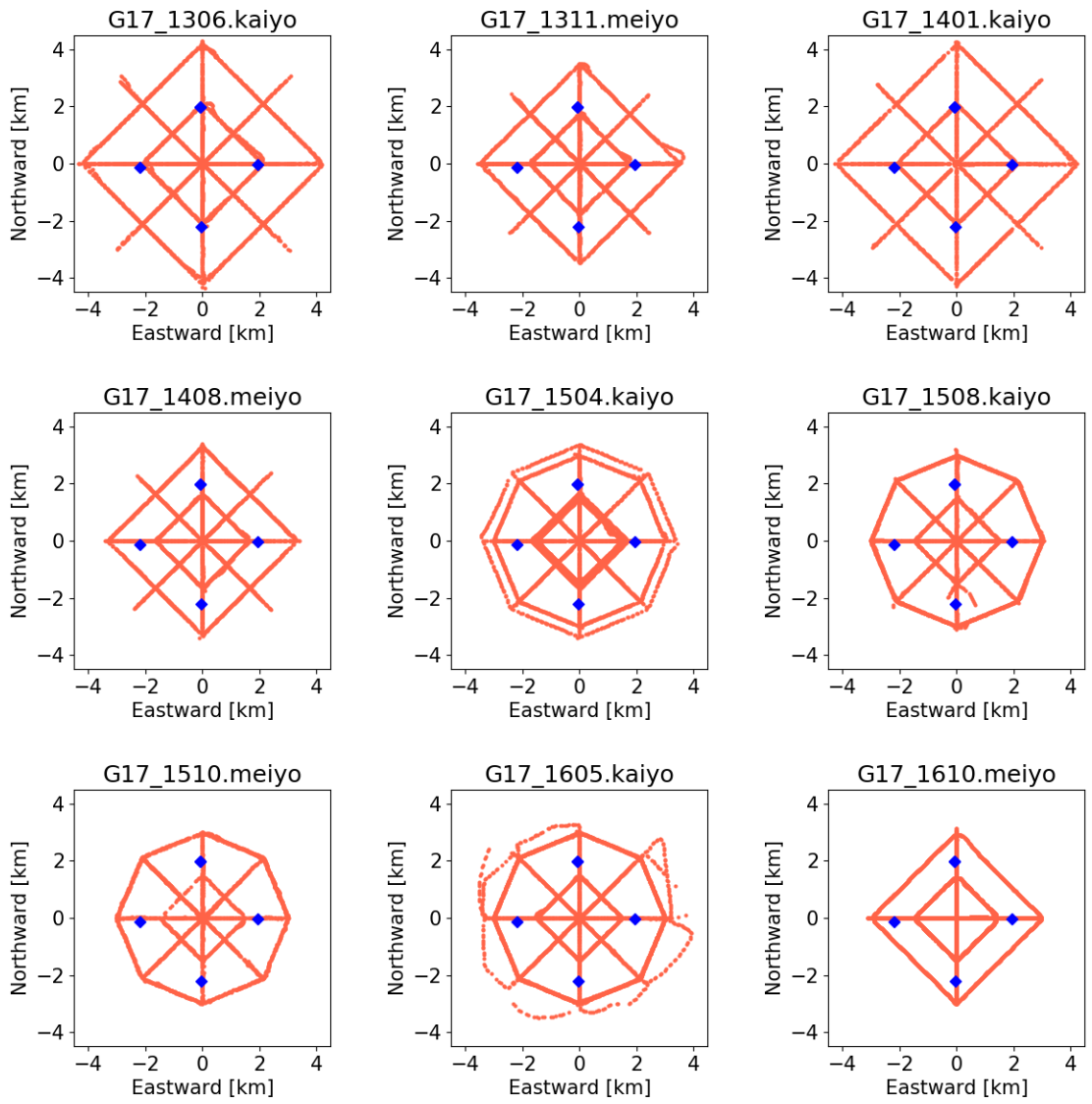

Fig. S4. Track lines at G17. Orange dots and blue squares indicate the positions of surface transponder for each acoustic data and seafloor transponders, respectively. Titles on each panel shows the 4-digit year-month and the name of the used vessel.

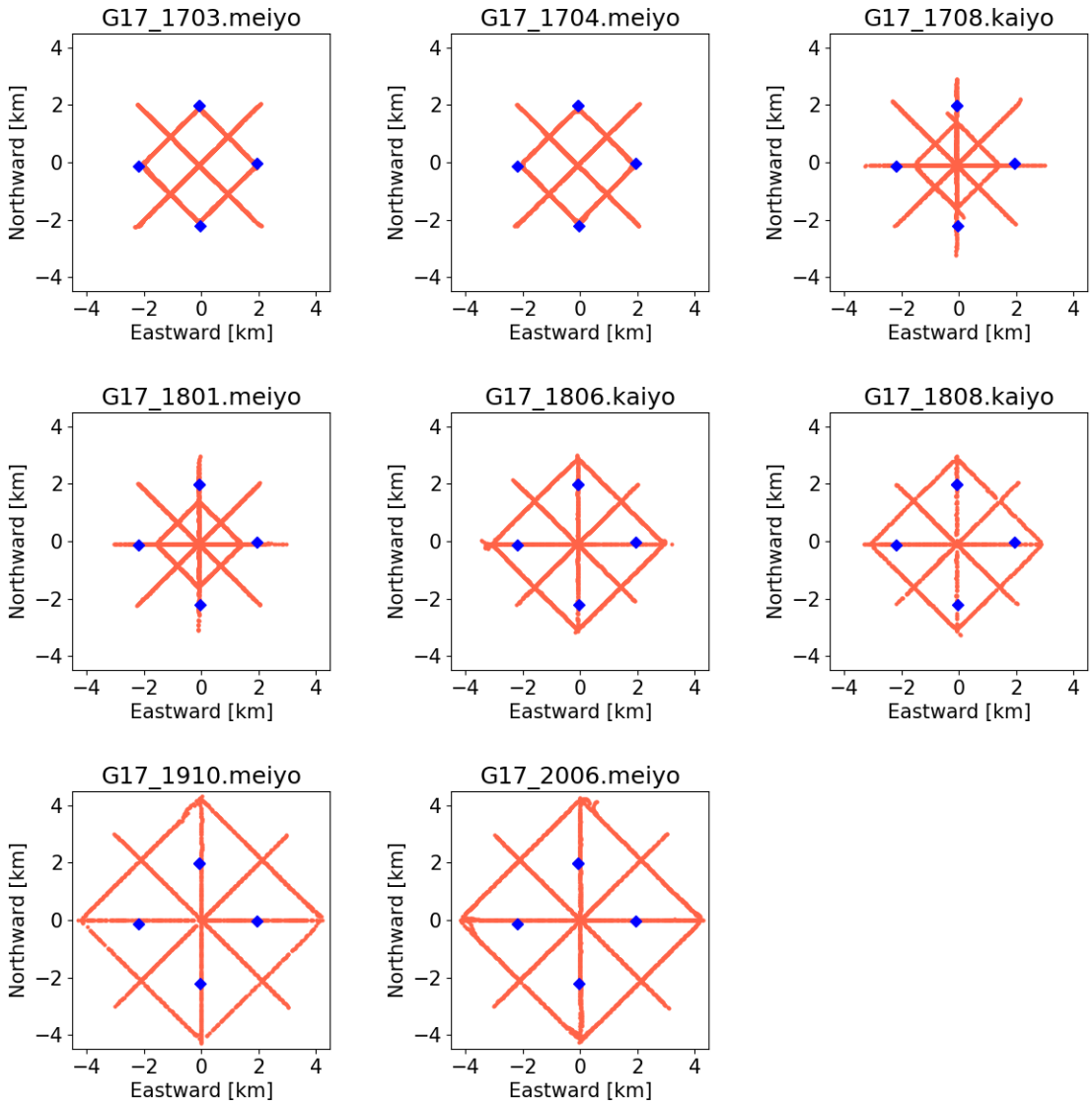

Fig. S4. Track lines at G17 (continued).

Data S1. (separate file)
Postseismic seafloor displacements with respect to the Eurasian plate of NUVEL-1A model *(11)*.

Data S2. (separate file)
Preseismic seafloor displacement with respect to the Eurasian plate of NUVEL-1A model *(11)*.